SPECIAL
Global Precipitation Measurement (GPM)
COLLECTION

Constructing a Multifrequency Passive Microwave Hail Retrieval and Climatology in the GPM Domain

SARAH D. BANG

NASA Postdoctoral Program, NASA Marshall Space Flight Center, Huntsville, Alabama

DANIEL J. CECIL

NASA Marshall Space Flight Center, Huntsville, Alabama

(Manuscript received 19 February 2019, in final form 28 May 2019)

ABSTRACT

Large hail is a primary contributor to damages and loss around the world, in both agriculture and infrastructure. The sensitivity of passive microwave radiometer measurements to scattering by hail led to the development of proxies for severe hail, most of which use brightness temperature thresholds from 37-GHz and higher-frequency microwave channels on board weather satellites in low-Earth orbit. Using 16+ years of data from the Tropical Rainfall Measuring Mission (TRMM; 36°S–36°N), we pair TRMM brightness temperature–derived precipitation features with surface hail reports in the United States to train a hail retrieval on passive microwave data from the 10-, 19-, 37-, and 85-GHz channels based on probability curves fit to the microwave data. We then apply this hail retrieval to features in the Global Precipitation Measurement (GPM) domain (from 69°S to 69°N) to develop a nearly global passive microwave–based climatology of hail. The extended domain of the GPM satellite into higher latitudes requires filtering out features that we believe are over icy and snowy surface regimes. We also normalize brightness temperature depression by tropopause height in an effort to account for differences in storm depth between the tropics and higher latitudes. Our results show the highest hail frequencies in the region of northern Argentina through Paraguay, Uruguay, and southern Brazil; the central United States; and a swath of Africa just south of the Sahel. Smaller hot spots include Pakistan, eastern India, and Bangladesh. A notable difference between these results and many prior satellite-based studies is that central Africa, while still active in our climatology, does not rival the aforementioned regions in retrieved hailstorm frequency.

1. Introduction

Severe hail results in billions of dollars in property damage each year, especially to crops, and to infrastructure in urban environments (Hohl et al. 2002; Changnon 2009). As of the end of 2018, insured losses in the United States due to severe convective storms have exceeded $10 billion for 11 consecutive years, and hail is the primary contributor to these losses (Aon Benfield 2018). The occurrence of hail with diameters >25 mm is a criterion in its own right for the U.S. National Weather Service to warn for a severe thunderstorm, and severe hail is often a harbinger of other violent weather to come (Bluestein and Parker 1993; Johns and Hart 1998).

Hailstorms' destructive potential and their place at the upper reach of the intensity spectrum of convective precipitation drives the need within the meteorological community to establish global hail climatologies, which can be constructed using either ground-report-based or remotely sensed approaches. While there are systems in place in some countries to report hail observed at the ground, the coverage of consistent surface reporting is far from global. Allen and Tippett (2015) note that biases in reporting due to population density and other societal or otherwise nonmeteorological factors present difficulties in using surface reports to build a hail climatology. Within the United States, the minimum required hail size to trigger a severe thunderstorm warning changed from 0.75 to 1.0 in. in 2010 (1 in. = 2.54 cm), leading to inconsistencies within the U.S. dataset itself

Denotes content that is immediately available upon publication as open access.

Corresponding author: Sarah D. Bang, sarah.d.bang@nasa.gov

DOI: 10.1175/JAMC-D-19-0042.1

over time. Furthermore, different countries have different reporting standards, thus leading to worldwide inconsistencies in hail reporting (Xie et al. 2008; Cecil and Blankenship 2012). Other ground-based hail climatologies include those based on ground-radar data, employing detection algorithms like maximum expected size of hail (MESH) (Cintineo et al. 2012; Schlie et al. 2019) or detection informed by dual-polarized radar data, fuzzy-logic hydrometeor identification (HID) schemes (Dolan and Rutledge 2009), or a combination of multiple detection parameters (Murillo and Homeyer 2019). A radar-based climatology, however, is inherently dependent on the accessibility of a widespread radar network and is limited to the geographic domain in which the radar network is operated.

The pitfalls of ground-based hail climatologies have instead motivated the development of satellite-based approaches, which would apply a consistent detection methodology to hailstorms the world around, covering countries where hail reporting or radar are sparse or nonexistent, and over the oceans. Based on the work of Spencer et al. (1987), the remote sensing community has leveraged passive microwave data from spaceborne radiometers to identify proxies for severe precipitation. The earlier works of Spencer et al. (1987, 1989) noted a strong correlation between reports of severe weather and 37-GHz passive microwave brightness temperatures (hereinafter T_b) lower than 200 K. Over a cloud, a ''depression'' of microwave T_b relative to the environment around it indicates that upwelling microwave emission is scattered away by ice particles in the column before reaching the radiometer (Spencer et al. 1987). Depressions in T_b above precipitating clouds can be used to estimate the volume of ice in the observed column, and the microwave frequency in which the depression is expressed can lend insight into the sizes of the ice particles therein (Vivekanandan et al. 1991).

Cecil (2009) put forth a technique to identify hail cores within convection using the 19-, 37-, and 85-GHz passive microwave channels from the passive microwave radiometer on board the Tropical Rainfall Measuring Mission (TRMM) satellite [the TRMM Microwave Imager (TMI)]. In both the 37- and 19-GHz channels, the likelihood of hail increased drastically with decreasing T_b. The relationships between reported hail at the surface and microwave T_b allowed Cecil (2009) to suggest T_b thresholds could then be applied to the microwave data to predict the probability of hail ($<$230 K for 19 GHz, $<$180 K for 37 GHz, and $<$70 K for 85 GHz). Using TRMM precipitation features (PFs, and myriad variations therein; Nesbitt et al. 2000; Cecil et al. 2005; Liu et al. 2008), Cecil (2011) found that of all PFs in the United States with a 37-GHz T_b below 220 K, 37% of them were associated with hail, and when applying a lower threshold of 180 K, this percentage increases to 60%. Higher-frequency (shorter wavelength) channels, such as those near and above 85 GHz, exhibit the same tendency for the likelihood of hail to increase with decreasing T_b, though the likelihood of reported hail at the surface maximizes around 50%, as the 85-GHz T_bs can be lowered efficiently by deep layers of ice particles smaller than hail (like graupel $<$ 5 mm) (Mroz et al. 2017).

Ferraro et al. (2015) applied T_b thresholds to 89, 150, and 183 $\pm$ 1/3/7-GHz data from the Advanced Microwave Sounding Unit (AMSU-A and AMSU-B) instrument matched with ground reports to create a hail climatology between the latitudes of 60°S–60°N, extending coverage beyond that of the TRMM satellite (36°S–36°N). Cecil and Blankenship (2012) applied weighted probabilities of 37-GHz T_bs to create fractional probabilities of hail, and used these probabilities to assemble a hail climatology using Advanced Microwave Scanning Radiometer for Earth Observing System (AMSR-E) data, which operated on board the sun-synchronous *Aqua* satellite.

Other satellite-based approaches combine passive microwave measurements with those from spaceborne radar, such as the precipitation radar (PR) on board TRMM, or the dual-frequency precipitation radar (DPR) on board the Global Precipitation Measurement (GPM) satellite. Ni et al. (2017) analyzed both radar and passive microwave data, comparing climatologies built using thresholds from both radar (44 dBZ at −22°C) and passive microwave (37 GHz below 230 K) data. Punge et al. (2017) developed a hail retrieval using infrared (IR) data from Meteosat Second Generation (MSG) satellites, applying an overshooting cloud-top detection algorithm developed by Bedka (2011) and Griffin et al. (2016) and used this retrieval to estimate a climatology of hail over Europe.

All of the aforementioned approaches use ground reports of hail to train their hail retrievals. Leppert and Cecil (2015) and Mroz et al. (2017) use instead ground radar dual-polarization hydrometeor identification instances of hail as the ''hail events'' upon which to train microwave retrievals. This approach provides a larger dataset than using ground reports, and sidesteps some of the potential errors of societal and geographic factors' influence on what is considered ''ground truth.'' Without a report of hail at the ground, however, an event designated as ''hail'' by the radar algorithm could be any size and anywhere in the vertical column (not necessarily at the ground), and if conditions allow, could melt while falling toward the surface.

While satellite-borne datasets provide a more uniform approach to building a global or near-global climatology, no method is without its disadvantages. Similar passive microwave T_bs can result from any number of combinations of layers of ice scatterers of different sizes, and different depths. Microwave T_bs are not unique to a single profile of scatterers (Toracinta et al. 2002). The footprint sizes relative to the ground of the passive microwave radiometers change with each instrument and each channel, and range from 6 km × 4 km (like the 183-GHz channels on board GPM) to 64 km × 37 km (like the 10-GHz channel on board TRMM) (see Table 1). The coarse resolution of instruments or channels with large footprint sizes can limit the amount of insight we can gain into convective scale phenomena like hailstorms or hail cores, as those phenomena tend to be on the order of kilometers. Mroz et al. (2018) note that virtually all microwave footprints containing hail exhibit nonuniform beamfilling (NUBF), in which a combination of hailing and nonhailing portions of the scene are represented. Though differing footprint sizes and different orbits complicate combination of microwave radiometer datasets from different satellite platforms, the microwave channels between 10 and 89 GHz are on board several weather satellites (*Aqua*, *MetOp-A* and *MetOp-B*, TRMM, and GPM, among many others). The platforms currently in orbit provide near-global coverage approximately every 4 h (Ferraro et al. 2015), further motivating the construction of accurate hail retrievals that rely solely on passive microwave data.

All of the climatologies discussed above yield relatively similar distributions across the globe, at least visually: well-known hail "hot spots" such as the central United States, northern Argentina, and the Bangladesh/eastern India region appear in each (Cecil and Blankenship 2012; Ferraro et al. 2015; Ni et al. 2017; Mroz et al. 2017). The most readily apparent differences, however, occur in the tropics, where different approaches represent hail to widely varying extents. In the climatologies of Mroz et al. (2017) and Ferraro et al. (2015), and the passive microwave–only climatology of Ni et al. (2017), we see hail heavily represented in the tropics (latitudes lower than ~15°), whereas Cecil and Blankenship (2012) applied regional scaling to mitigate this effect. The radar-based climatology of Ni et al. (2017) depicted substantially less hail in the tropics than in the passive microwave climatology. In the tropics, the troposphere is deeper than at higher latitudes, and therefore tropical clouds have a deeper layer in which to grow, relative to subtropical and midlatitude clouds. A deep layer of ice that is small enough to melt while falling may have a similar T_b to a shallower layer of larger hail-sized ice. It is also plausible that retrievals trained on hail anywhere in the vertical column and not just at the surface, like that of Leppert and Cecil (2015) and Mroz et al. (2017), could identify hail in the tropics that would melt before reaching the surface, if the column were dominated by smaller hail and graupel.

TABLE 1. Footprint sizes (km) of the channels of the TRMM Microwave Imager and GPM Microwave Imager used in this paper. For more detail on the TMI and GMI instruments and their footprints, see Kummerow et al. (1998) and Hou et al. (2014), respectively.

Frequency (GHz)		Footprint (km)	
TMI	GMI	TMI	GMI
10.65	10.65	63 × 37	32 × 19
19.35	18.7	30 × 18	18 × 11
37.0	36.5	16 × 9	15 × 9
85.5	89.0	7 × 5	7 × 4
	183 ± 3/7		6 × 4

Among other potential limitations, hail retrievals trained in one location (often the United States) may not translate to other locations around the globe. Cecil and Blankenship (2012) attempt to mitigate this issue by applying regional scaling factors to different regional boxes throughout the AMSR-E domain. Those scaling factors are based on empirical relationships between T_b and radar profiles in each region. Surface snow or ice cover can be a major problem for retrievals at high latitudes, or over mountains. Icy or snow-covered surfaces can exhibit very low microwave T_bs (Skofronick-Jackson and Johnson 2011; Ebtehaj and Kummerow 2017), occupying the same T_b regimes as intense hailstorms. This can be seen in the strong representation of hail in central Greenland in the climatology of Ferraro et al. (2015), where there is likely not a high concentration of severe hail.

All of the aforementioned factors are challenges faced by those building satellite-based hail climatologies, and the application of different mitigating effects and filters depends ultimately on the prioritization of maximizing probability of detection (POD), minimizing false alarm rate (FAR), or any other metric of success. Since storm types that are relatively easy to detect, or prone to triggering false alarms, are likely not to be distributed evenly, choices based on a given metric of success affect the resulting retrieved patterns. Ferraro et al. (2015) favored a high POD and their retrieval likely triggered on many subsevere thunderstorms in tropics, for example. Cecil and Blankenship (2012) favored a lowered FAR, and consequently their retrieval may have missed a large number of hail events.

This paper builds on the passive microwave–based climatologies in the literature (Cecil and Blankenship 2012; Ferraro et al. 2015; Ni et al. 2017). We aim to

construct a nearly global climatology of hail throughout the GPM domain, mitigating where possible the effects of surface snow and ice, and the variation in troposphere depth between the tropics and high latitudes. The paper is organized as follows: the following section (section 2) details the TRMM and GPM precipitation feature databases that we construct, and the hail ground reports to which these databases are matched. In section 3, we discuss the training of a hail retrieval on United States ground hail reports paired with TRMM features, which we use to estimate hail probabilities using passive microwave T_b variables from the channels near 10, 19, 37, and 85 GHz. In section 4b we explain the development of a passive microwave–based filter to remove signals from ice, snow, and liquid water from GPM-based features. Finally, we apply our multifrequency hail probability estimates to filtered GPM features to construct a hail climatology throughout the GPM domain (section 5).

2. Data

For this analysis, we make use of a modification of the TRMM and GPM satellite polarization corrected temperature features (TPCTF and GPCTF, respectively) databases. These are precipitation features (Nesbitt et al. 2000; Liu et al. 2008) contained within a contiguous area with 85-GHz (TRMM) and 89-GHz (GPM) polarization corrected brightness temperature (PCT, Spencer et al. 1989) at or below 200 K as viewed by the TMI or GPM Microwave Imager (GMI) [Precipitation Processing System (PPS) 2014; Berg 2016; Iguchi and Meneghini 2016]. PCTFs range in size from 1 TMI pixel (35 km^2) to thousands of square kilometers. PCTFs with hail, or with a high estimated probability of hail, tend to have areas in the hundreds of square kilometers.

Data products titled "TPCTFs" and "GPCTFs" are available to the public online (http://arthurhou.pps.eosdis.nasa.gov); however, these are defined using a minimum 85-GHz (89 GHz for GPM) PCT of 250 K, instead of the 200 K used in this paper. For this analysis, we note that we added maximum 10-, 19-, 37-, and 85- (89) GHz PCT to the variables already saved for these features.

We match the TPCTFs in the U.S. subdomain to Storm Prediction Center archived and quality-controlled hail reports for the years 1997–2014 (the entirety of the TRMM lifetime) (PPS 2014). These reports are mostly based on storm spotters in the general public. The minimum hail size reported usually corresponds to the U.S. National Weather Service threshold for a severe thunderstorm (18 mm before 2010, 25 mm after 2010) (Allen and Tippett 2015). We match the latitude and longitude of a hail report to the coordinates of the TPCTF's minimum 37-GHz PCT, within 100 km of the hail report and within ±1 h. If there are multiple TPCTFs tagged to a hail report, the feature with the lowest 85-GHz PCT is assigned to the hail report, and the other nearby TPCTFs within the swath are removed from consideration in the hail probability calculations, to avoid convoluting the probability calculation. It is on this subset of U.S. TPCTFs that we perform our hail retrieval training.

The TPCTFs used for matching to the U.S. ground hail reports are taken from between 30.5°N and the upper bound of the TRMM orbit, ~36°N latitude, and 105° and 81.5°W longitude. This excludes regions with frequent snow and ice cover that can have signatures similar to hail. The box also excludes oceans and the Great Lakes, where there are no surface hail reports. The climatology mapping is performed on GPCTFs in the entire GPM domain, from 69°S to 69°N.

In section 4b we examine a subset of the GPCTFs that lie within the Ku swath of the GPM DPR. We then employ the concurrent radar data within this subset of GPCTFs to identify which features are erroneously marked as "hailing" when there is little or no accompanying radar signature.

As previously mentioned, high tropopause heights may support tall storms with scattering signatures resulting from a deep layer of graupel, rather than hail. In section 3, we normalize 37-GHz brightness temperature depressions by the height of the tropopause. The tropopause height is estimated using the World Meteorological Organization (WMO) 1957 definition of the lapse-rate tropopause (LRT), that is, "the lowest level at which the lapse rate decreases to 2°C/km or less" (World Meteorological Organization 1957, p. 137). These heights are estimated using European Centre for Medium-Range Weather Forecasts (ECMWF) interim reanalysis data (ERA-Interim; Dee et al. 2011; Berrisford et al. 2011) (ECMWF 2018). The search for the LRT begins at 5-km altitude, and defaults to a cold-point tropopause if a sufficient lapse rate is not found. This calculation was employed by Liu and Liu (2018), who have provided the ERA-Interim-derived LRT heights used in this paper.

3. TRMM feature-based hail probability estimation

As seen in Cecil (2009), the percentage of TRMM precipitation features with reported hail increases precipitously with decreasing 19-, 37-, and 85-GHz PCT. We emulate the Cecil (2009) Fig. 2 here, using our TPCTF dataset, showing the fractions of TPCTFs with (reported) hail for binned minimum 19-, 37-, and 85-GHz PCTs (Fig. 1).

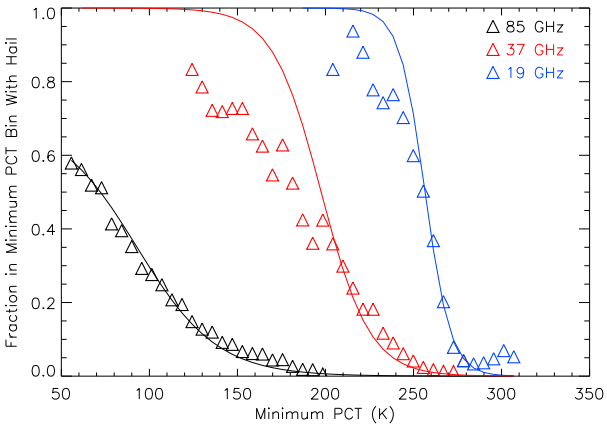

FIG. 1. Percentage of TRMM PCTFs with reported hail at the surface for binned values of minimum 85- (black), 37- (red) and 19-GHz (blue) polarization corrected brightness temperature. Lines overlaid on top of each curve correspond to the logistic-curve fits expressed in Table 2.

These gradients of hail probability with decreasing microwave brightness temperature led Cecil (2009, 2011), Cecil and Blankenship (2012), Ferraro et al. (2015), and others to create brightness temperature thresholds for hail (like <230 K for 19 GHz, <180 K for 37 GHz, and <70 K for 85 GHz; Cecil 2009). Instead of setting a firm threshold, we instead regressed a probability curve to the data. Linear regression provided unrealistic hail probabilities at high brightness temperatures, and the oscillatory nature of a polynomial fit predicted probabilities that would rebound from zero as the graph continued to higher brightness temperatures. These forms of regression yielded unrealistic probability distributions. We chose instead to fit logistic curves of the form

$$f(x) = \frac{L}{1 + e^{-k(x-m)}} \tag{1}$$

to the hail probabilities, where L is the maximum probability value (in most cases 1, or 100% probability), m is the midpoint of the sigmoidal curve, and k is the steepness of the curve.

The fit of the probability curve is highly dependent on the bin widths along the abscissa. To avoid any unintentional bias, we calculate the bin widths on the basis of Scott (1979) and present them in Table 2.

Values for the three terms [L, k, and m; see Eq. (1)] of the logistic fits for several variables are shown in Table 2. These variables include T_b minima and T_b depressions relative to a background T_b. Figure 2 shows the hail probabilities and their logistic fits for two variables that are emphasized throughout this paper and are defined below. At the high end of hail probabilities, these fits overestimate the observed values. This overestimation is intentional, as the underlying database of hail observations is subject to underreporting, with some true hail occurrences missing because of geographic or other factors (Cecil 2009; Allen and Tippett 2015).

TABLE 2. Logistic-curve parameters L, k, and m [Eq. (1)] for the passive microwave T_b variables used in this paper, and the bin widths of their histograms, calculated based from the formula of Scott (1979).

	Logistic-curve-fit parameters			
	L	k	m	Bin width
Min 19-GHz PCT	1	−0.137	257	2.63 K
Normalized 37-GHz PCT depression	1	0.762	5.09	0.322 K km^{-1}
37-GHz PCT depression (max 37-GHz PCT − min 37-GHz PCT)	1	0.0470	75.9	6.99 K
Min 37-GHz PCT	1	−0.0723	196	3.77 K

We present *normalized 37-GHz PCT depression* in Table 2, defined as

$$\text{Normalized 37-GHz PCT Depression} = \frac{\text{MAX37PCT} - \text{MIN37PCT}}{(\text{LRT})}, \tag{2}$$

where MAX37PCT is a feature's maximum 37-GHz PCT (K), MIN37PCT is the minimum 37-GHz PCT (K), and LRT is the ERA-Interim-derived lapse-rate tropopause height (km) (see section 2). For higher tropopauses, this normalization reduces the value of a feature's T_b depression.

Normalized 37-GHz PCT depression has units of K km^{-1}. It is an improvement over simply using the minimum 37-GHz PCT, because it accounts for storms occurring over a variety of background scenes (whether radiometrically warm or cold). Because we are looking at maxima–minima differences, this automatically excludes from our dataset small TPCTFs and GPCTFs that are constituted of only one TMI or GMI pixel, respectively.

The minimum 37-GHz PCT or its T_b depression is a common proxy for severe weather and hail (Spencer et al. 1987), and this relationship is well known. We show the relationship between TRMM features' minimum 37-GHz PCT and hail in Fig. 1. In Fig. 2a, we quantify the 37-GHz PCT depression by subtracting the features' minimum 37-GHz PCTs from their maxima and normalize the depression by the depth of the troposphere.

We also present the logistic-curve fits for the *minimum 19-GHz PCT* in Table 2. This is the minimum observed PCT within the boundaries of a TPCTF (see section 2). Cecil (2009) showed a sharp response in hail probability as TMI 19-GHz brightness temperature

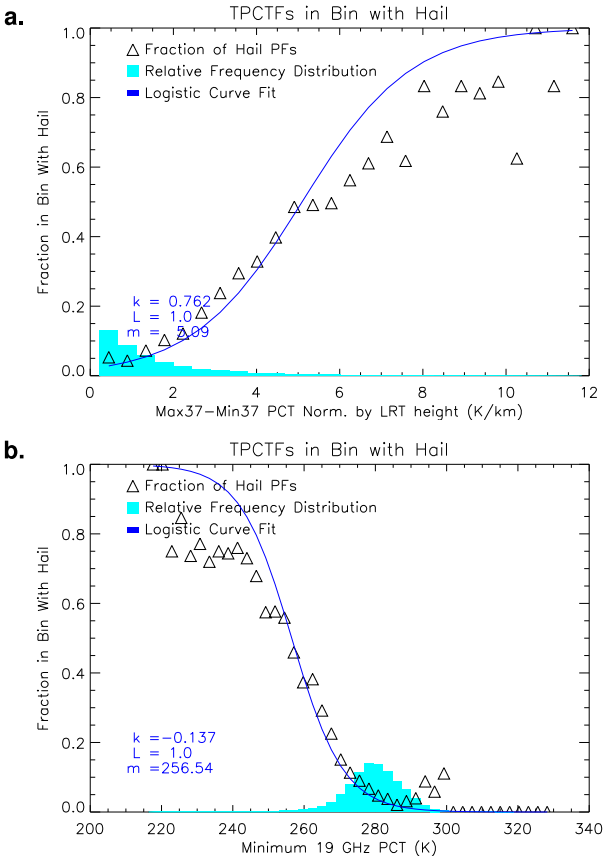

FIG. 2. Fraction of TPCTFs with hail (symbols) and relative frequency distribution (shading) for binned values of (a) normalized 37-GHz PCT depression and (b) minimum 19-GHz PCT. Solid lines are logistic-curve fits from Eq. (1) and Table 2. The parameters of the curve fits are printed in the lower-left of each panel. The data here are prescreened by the snow/ice filters discussed in section 4b.

decreases. The higher spatial resolution for the 19-GHz channel on GMI than on TMI, and the development of 19-GHz PCT coefficients by Cecil and Chronis (2018) suggest the use of this frequency is more promising now for hail detection than it had been previously. Mroz et al. (2017) note that, when microwave channels on board GPM are examined individually, and independently of the GPM DPR radar, the 19-GHz channel presents the greatest potential for hail detection of all of the available microwave channels. We find a similarly strong relationship between the TRMM minimum 19-GHz PCT of a TPCTF and the frequency of reported severe hail, which we present in Fig. 2.

Plotted in blue over the distributions of hail probability in Fig. 2 are the fitted logistic curves we calculate for both normalized 37-GHz PCT depression and minimum 19-GHz PCT as in Eq. (1). The three terms of the equation, L, k, and m, are presented on the figure, as well as listed in Table 2.

To extract more information about the ice scatterers within the features, we can combine the estimated probabilities for TPCTFs using the 19- and 37-GHz channels simultaneously (Fig. 3). The sample size for a given combination of minimum 19-GHz PCT and normalized 37-GHz PCT depression can be small, so we combine the probabilities that are derived from those terms individually. For every TPCTF, we estimate the probabilities of hail based on minimum 19-GHz PCT and normalized 37-GHz PCT depression using Table 2. Then we take the square root of the product of those individual probabilities. This better accounts for cases where one metric suggests a much higher probability of hail than the other. In those cases, the higher probability is usually suspicious (perhaps an artifact related to snow cover on the ground). For example, if the hail probability calculated using normalized 37-GHz PCT depression is 90%, while for minimum 19-GHz PCT it is 10%, the square root of the product of the probabilities yields a 30% estimated probability of hail. The combined probability using the square root tends toward the smaller of the two individual probabilities.

4. Application to GPM

a. *Histogram adjustment to account for resolution differences*

The 19-GHz footprint of the GMI is much smaller than that of TMI (see Table 1), and is thus capable of measuring lower PCT values with less nonuniform beamfilling. We apply a histogram-matching procedure to account for this, based on distributions of 19-GHz PCT measured in a 20°S–20°N domain having comparable sampling by both TMI and GMI. This leads to computing a TMI-equivalent PCT value $\mathrm{PCT19_{TMI}}$ from the measured $\mathrm{PCT19_{GMI}}$, as

$$\mathrm{PCT19_{TMI}} = \begin{cases} [1.49 - 0.0018(\mathrm{PCT19_{GMI}})]\mathrm{PCT19_{GMI}} & \text{if} \quad \mathrm{PCT19_{GMI}} \le 272\,\mathrm{K} \\ \mathrm{PCT19_{GMI}} & \text{if} \quad \mathrm{PCT19_{GMI}} > 272\,\mathrm{K} \end{cases}. \tag{3}$$

This effectively scales up the measured $\mathrm{PCT19_{GMI}}$ by a factor that is itself a function of $\mathrm{PCT19_{GMI}}$. Applying Eq. (3) to a 250-K measurement from GMI, for example, would give a TMI-equivalent value of

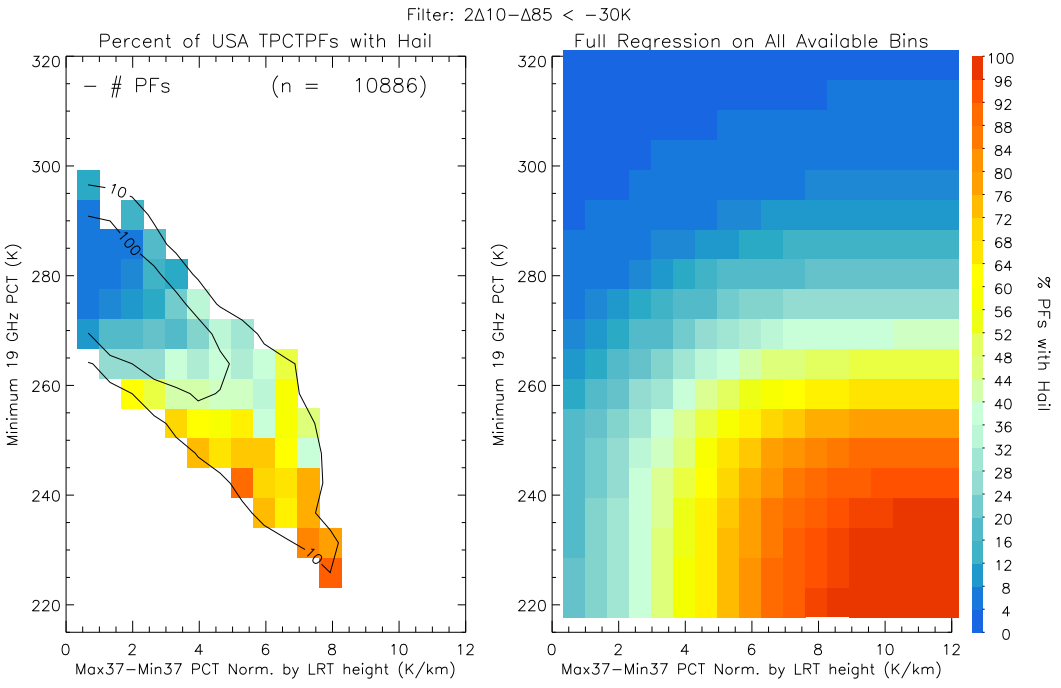

FIG. 3. (a) Percent of TPCTFs with hail (color shading) and total TPCTF count (line contours) for each two-dimensional bin of minimum 19-GHz PCT and normalized 37-GHz PCT depression. (b) Two-dimensional probability of hail as estimated from the square root of the product of the probabilities estimated individually from minimum 19-GHz PCT and normalized 37-GHz PCT depression.

260 K. Using $x = 260$ K in Eq. (1), this gives an estimated hail probability of 40%. A 200-K measurement from GMI would equate to 226 K for TMI, giving a 99% probability of hail from Eq. (1).

No histogram matching is applied to the higher-frequency channels, because their footprint sizes are comparable between GMI and TMI. There is a large difference in footprint size for the 10-GHz channels on GMI and TMI, but we use those channels for screening out surface snow and ice scenes. Those scenes tend to be much larger than the footprint from either satellite, so we do not adjust the 10-GHz measurements.

b. *GPM feature filtering*

As can be seen in the high estimated concentration of hail over Greenland in the AMSU climatology of Ferraro et al. (2015), when using passive microwave data only (and not including any other radar, surface, or environmental data), snowy or icy surfaces may falsely register as "hail" to a retrieval. The much wider range of latitudes surveyed by the GPM satellite (69°S–69°N) presents the challenge wherein sea ice and other ice- and snow-covered surfaces must be accounted for in precipitation retrievals. As in Ferraro et al. (2015), our preliminary methods retrieved high concentrations of hail over Greenland, and also over the Antarctic Peninsula. There are also regions where there is high-altitude terrain in close proximity to regions that experience severe weather, such as near the base of the Himalayas and the central United States. In these regions, radiometric signatures from both severe convective phenomena and surface snow regimes would be possible.

To create an effective filter for artifacts erroneously identified as hail, we examine some key radiometric variables for GPCTFs in some of the problematic regions discussed above (Fig. 4: the Antarctic Peninsula, Himalayas, Mongolia, and Europe) and compare them to our United States region, and to the entire GPM domain. We analyze a subset of our GPCTF dataset in Fig. 5 using features that lie only within the Ku swath of the GPM DPR. This way, we can analyze the concurrent radar data of the features identified in microwave imagery to determine whether the features are representative of deep convection, or of a surface artifact. The points for the GPCTFs plotted in Fig. 5 are those whose estimated probability of hail is over 20% based on minimum 19-GHz PCT and normalized 37-GHz PCT depression, a threshold used in our climatology to follow. The points are colored by maximum Ku-band reflectivity at the −10°C level, as an indicator of the relative intensity of the features in the different regimes.

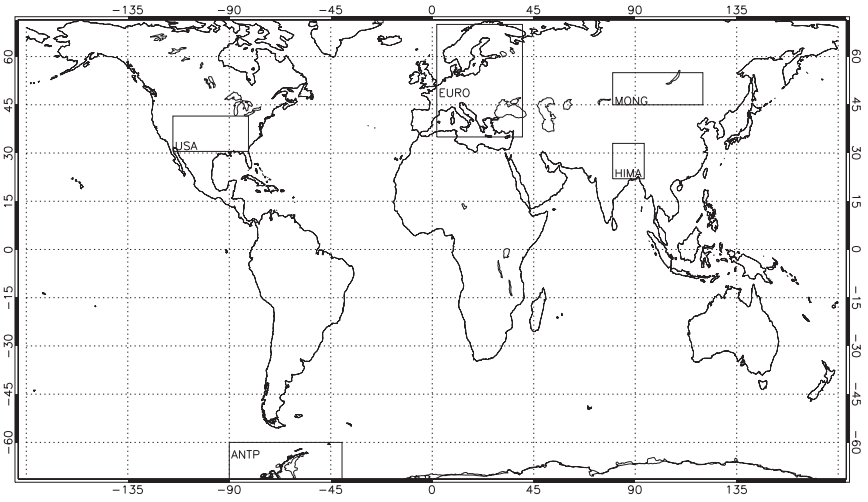

FIG. 4. Map of the GPM satellite domain (69°S–69°N), overlaid with boxes outlining the five regions we discuss in section 4b: United States (USA), Antarctic Peninsula (ANTP), Europe (EURO), Mongolia (MONG), and the Himalayas (HIMA). Note that all of the boxes save for the Antarctic Peninsula comprise a diverse set of features, containing those we expect to have legitimate hail and those we suspect are snow scenes.

In Fig. 5, we examine a radiometric variable that shows a strong signal in the problematic regimes shown on the map in Fig. 4 and discussed above. Our radiometric "filter" variable was created following the logic put forward by Ebtehaj and Kummerow (2017), who found that combining values from low-frequency (10–19 GHz) and high-frequency (89–166 GHz) channels provided the best information with which to detect snowfall over snowy surfaces. This filter, which is plotted along the x axis of the panels in Fig. 5, is

$$2\Delta10 - \Delta89 = 2(\text{MAX10PCT} - \text{MIN10PCT}) - (\text{MAX89PCT} - \text{MIN89PCT}), \quad (4)$$

where MAX10PCT is a feature's maximum 10-GHz PCT and MIN10PCT is its minimum, and likewise for 89-GHz PCT, for GPCTFs (85 GHz for TPCTFs). The $2\Delta10 - \Delta89$ has units of kelvin (K). A convective storm gives a much larger depression in the high-frequency channels than in the low-frequency channels, making $2\Delta10 - \Delta89$ negative. A snow- or ice-covered surface has large depressions from the background for both. The 10-GHz channel has the largest footprint relative to the other channels, and its extinction coefficient is the least responsive to scattering by most spherical ice particles of the available channels (see Mroz et al. 2017, their Fig. 6). Because of this, MAX10PCT represents more of the background than MAX89PCT. As a result, the MAX10PCT − MIN10PCT term tends to be larger than the MAX89PCT − MIN89PCT term for snow- and ice-covered features, and the $2\Delta10 - \Delta89$ value is usually greater than −30 K for snow and ice surfaces.

Sea ice regimes, like those of the Antarctic Peninsula, dominate the higher end of the $2\Delta10 - \Delta89$ spectrum. By contrast, the GPCTFs over the United States lie clustered below −30 K for $2\Delta10 - \Delta89$. Regions like Mongolia, the Himalayas, and the Europe boxes we identify in Fig. 4 contain both snow scenes and legitimate features we would expect to have hail. Examining each of these regions in Fig. 5, there is a strong demarcation in $2\Delta10 - \Delta89$ around −30 K between features with no radar signature (black dots) or a weak (<30 dBZ) maximum reflectivity at the −10°C level (light blue and green dots) and features with a strong (>30 dBZ) radar signature at −10°C. Examining the $2\Delta10 - \Delta89$ metric for features throughout the entire GPM domain, in the lower-right panel of Fig. 5, the −30-K threshold separates strong radar reflectivities from weak or nonexistent radar reflectivities for almost all features, with only a small amount of features with strong reflectivities at −10°C that would "fail" the snow filter.

Our filter entails the removal of TPCTFs and GPCTFs with $2\Delta10 - \Delta89 > -30$ K (the dashed vertical line on the panels of Fig. 5), although we include any feature whose minimum 85 (89 for GPM) GHz PCT falls below 120 K (the dashed horizontal line). All of the hail probability plots we show (Figs. 2 and 3) are for TPCTFs that remain after we have applied this filter. This filter is an alternative to the method put forth by Grody (1991) and used by Cecil and Blankenship (2012). Cecil and Blankenship (2012) also removed cases with minimum

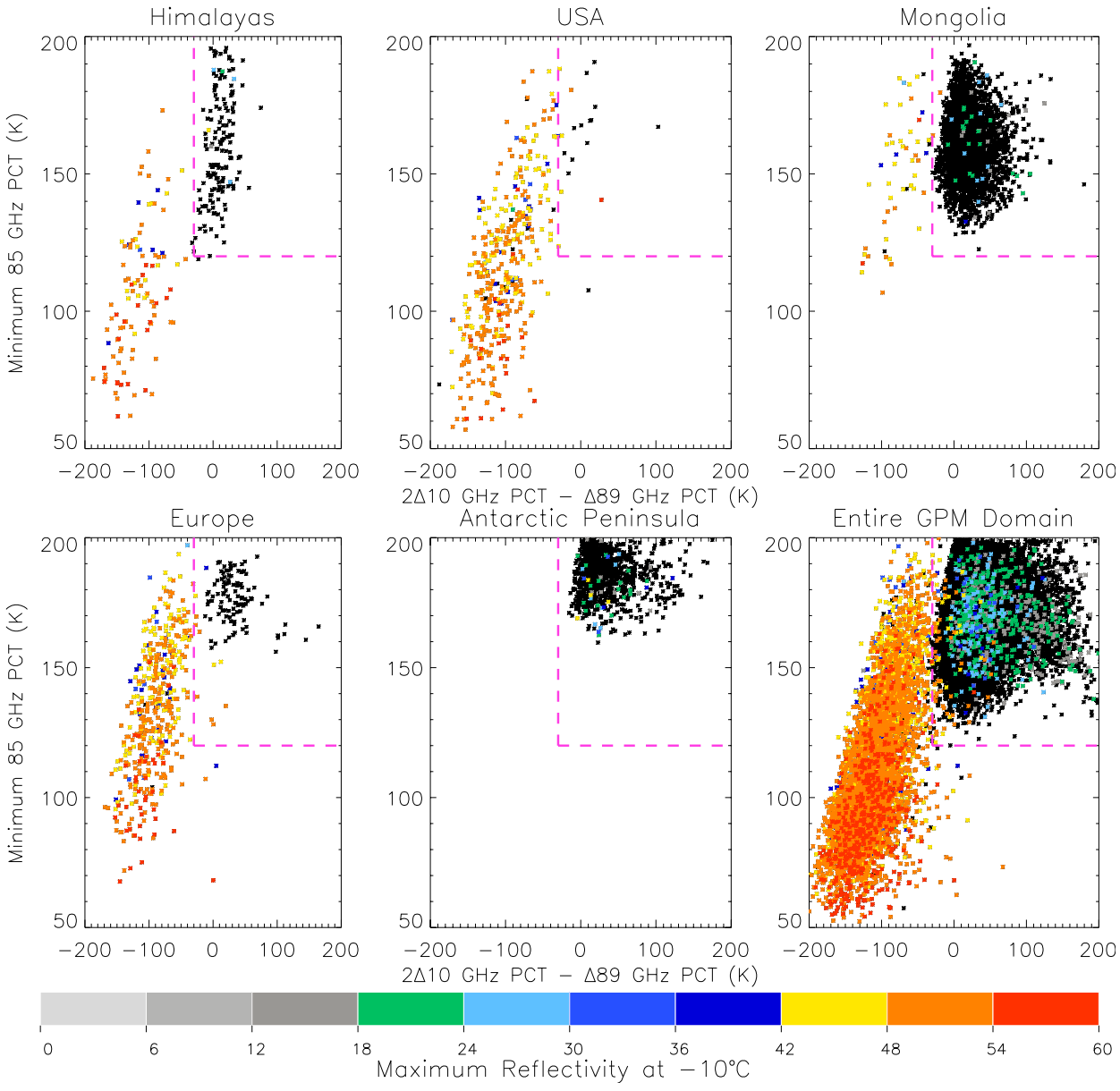

FIG. 5. Scatterplots of minimum 89-GHz PCT vs $2\Delta10 - \Delta89$ [see Eq. (4)] for the five regions shown in Fig. 4 and the entire GPM domain. The features presented are a subset of the GPCTFs contained within the Ku swath of the GPM DPR radar (see section 4b). The color of the points corresponds to the bins of maximum Ku-band reflectivity at the −10°C level, shown at the bottom. The snow/ice filtering threshold we propose in section 4b is depicted with a dashed pink line: $2\Delta10 - \Delta89 > -30$ K, and any feature with a minimum 89-GHz PCT below 120 K is also included.

89-GHz PCT over 130 K. That was essentially a brute force removal of potential snow- and ice-covered artifacts, which we find to be too restrictive. The filter presented here appears to be effective for removing surface-based artifacts while retaining the most intense convective storms.

An effective filter can also be constructed by subtracting from the 10-GHz depression a depression of T_bs from the 183 ± 3/7-GHz channels on board GPM instead of 89 GHz. The 183-GHz channels have the smallest footprint among those on GPM (see Table 1), and, because they are water vapor channels, the 183-GHz channels are sensitive to scattering at cloud level but less so to effects from the surface (Skofronick-Jackson and Johnson 2011). We choose to present the $2\Delta10 - \Delta89$ filter because GPM is the only satellite currently in orbit with both the 10- and 183-GHz channels, whereas the channel set from 10 to 89 GHz exists on many other platforms. With careful

adjustment to account for differences in orbit and footprint size, this filter and the results from this paper may subsequently be applied to large datasets from other satellites with similar combinations of microwave frequencies.

c. *Hail-event frequency normalization*

Generating maps of derived hail-event frequency involves estimating the number of observed events for each grid box, and normalizing by the number of opportunities for the orbiting satellite to observe each grid box. Here the number of observed events is actually an accumulation of fractional hail probabilities (as in Cecil and Blankenship 2012; Mroz et al. 2017) instead of a count of yes/no hail detections (as in Ferraro et al. 2015; Ni et al. 2017). The number of opportunities to observe a grid box involves irregular temporal sampling resulting from the satellite's low-Earth orbit and sometimes partial sampling near the edge of the satellite's observational swath. The derived hail-event frequency is computed on a 1° × 1° latitude–longitude grid as summarized by Eq. (5), with its terms described below:

$$\underbrace{\frac{\text{Accumulated Hail}}{\text{All Years}}}_{(1)} \times \underbrace{\frac{\text{No. Hail PFs}}{\text{No. Filtered Hail PFs}}}_{(2)} \times \underbrace{\frac{4\ \text{Normalized Passes/Day}}{\text{No. Passes/Day}}}_{(3)} \times \underbrace{\frac{10^4\ \text{km}^2}{\text{Box Area (km}^2\text{)}}}_{(4)} \tag{5}$$

1) Term 1: The first term is an estimate of the number of hailstorms observed per grid box. For a given 1° × 1° grid box, the fractional hail probabilities are summed for all GPCTFs (April 2014–March 2018) that are estimated to have at least 20% probability of hail. This 20% minimum is applied in order to avoid giving undue weight to the vast number of apparently weak storms that have a nonzero chance of hail. Without applying some such minimum, regimes with frequent weak-to-moderate convection [e.g., the intertropical convergence zone (ITCZ)] generate unrealistically high hail-event counts. This minimum probability can be adjusted higher or lower, depending on one's tolerance for false alarms.
2) Term 2: The second term is a scaling factor to account for the inability of our satellite-based methods to recognize all hailstorms. The training dataset (storm reports of severe thunderstorms with large hail in the United States; section 2) includes some observed hail events that themselves would not be counted in term 1's accumulation of fractional hail probabilities. GPCTFs that fail the filters for surface snow or ice are excluded, and those with computed hail probabilities below 20% are excluded. Term 2 is the ratio of the number of observed hail events in the training sample to the number of those observed hail events in the training sample that meet the criteria for inclusion in term 1. This term effectively scales the result such that the derived hail-event frequency does not drastically increase or decrease simply because of changes in the aggressiveness of a filter. For example, if we decreased the minimum probability in term 1 to 10%, more GPCTFs would be included in the summation in term 1, but the total number of derived hail events would be similar. An increase in derived storm counts in the ITCZ, where there are many low-probability storms, would be countered by decreases elsewhere.
3) Term 3: The third term is a scaling factor to account for nonuniform sampling by the satellite. For each 1° × 1° grid box, we count the number of GPM orbits that fully or partially sampled that grid box with the GMI instrument. Partial sampling of a grid box along the edge of a satellite swath is treated by subdividing into sixteen 0.25° × 0.25° boxes and counting what fraction of those had a valid GMI data point for that orbit. This effective total number of GMI observations is in the denominator for term 3. Dividing the first two terms by this denominator would essentially give the estimated number of hail events per GPM overpass. Following Cecil and Blankenship (2012), we also multiply (as the numerator of term 3) by a hypothetical sampling rate of four observations per day. This is intended to estimate how many storms would be seen with 6-hourly sampling every day. The appropriate desired sampling rate here is debatable. Discrete hail events can certainly occur more frequently than every 6 h, but with a very high sampling rate (e.g., geostationary imagery updating on the order of minutes) we would be double counting individual events. Since our passive microwave–based methods are best suited to intense mesoscale systems, we tend toward a mesoscale time period here.
4) Term 4: The fourth term normalizes each latitude–longitude grid box by a uniform size of 10^4 km^2.

In the climatologies in the section to follow, we calculate the accumulated probability of hail, normalized using the procedure discussed above, for filtered (section 4b) GPCTFs (domain: from 69°S to 69°N). The probability of hail is estimated for each GPCTF using both the minimum 19-GHz PCT and normalized 37-GHz PCT depression variables, taking the square root of the product of their hail probability as estimated using

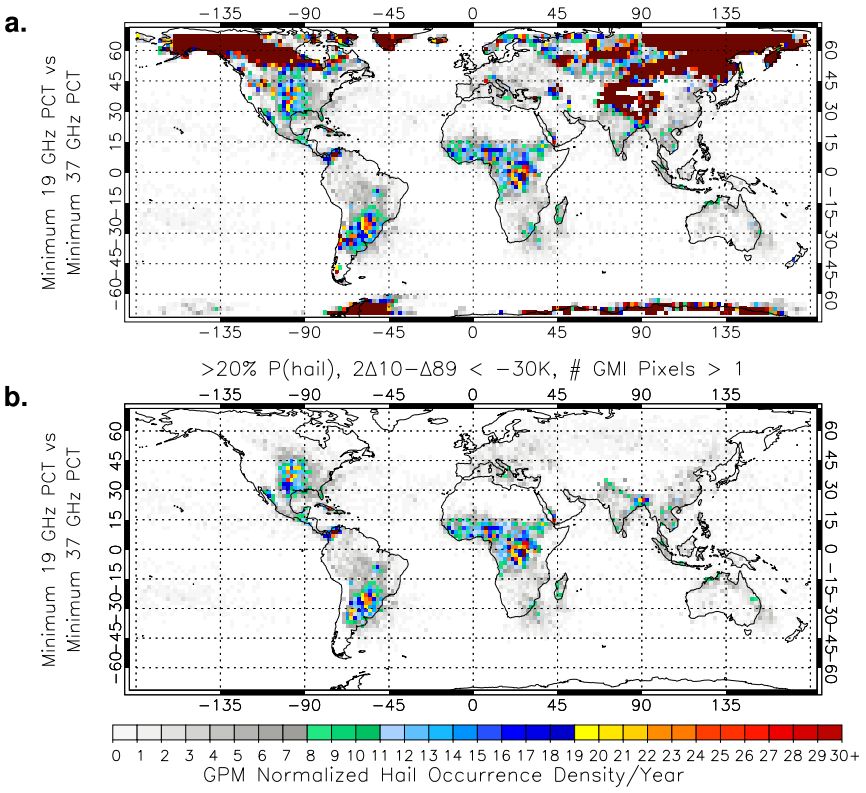

FIG. 6. Climatologies of hail in the GPM domain from April 2014 to March 2018. Values presented are of accumulated probability of hail (>20%) as estimated using (histogram adjusted; section 2) minimum 19-GHz PCT and minimum 37-GHz PCT normalized by GPM overpasses and by box area (section 4c). Values have been averaged into 2° × 2° boxes for smoothness. We present the same climatology in both panels, (a) without snow/ice filtering and (b) with filtering. A description of the snow/ice filtering process can be found in section 4b.

the logistic-curve fit parameters outlined in Table 2 and Fig. 2.

5. Hail climatology

In Figs. 6 and 7, we present three separate maps to illustrate some of the different approaches to estimating hail probability that we have taken in this paper. Each map shows the estimated yearly hail frequency over the GPM domain, using different filtering approaches (see section 4b) and different passive microwave variables for fitting the hail probability curve (see Table 2 for the variables' different curve fit parameters).

In Fig. 6 we examine in both panels the hail climatologies for GPCTFs estimated using minimum 19-GHz PCT and minimum 37-GHz PCT and compare the results without a snow/ice filter (Fig. 6a) with those with the filter applied (Fig. 6b). Note in Fig. 6a the incredibly high estimated frequency of hail over high latitudes, snow, and sea ice regimes. As snowy and icy surface regimes have large brightness temperature depressions in the microwave, it is readily apparent from Fig. 6a that a filter is needed to eliminate GPCTFs in these regimes that are likely not hailing but are yielding a falsely high probability of hail. The Himalayas are especially problematic because of the frequency of intense storms in adjacent parts of India, Pakistan, and Bangladesh.

Hail climatologies based on TRMM (from 36°S to 36°N) in the literature do not include many high-latitude ice regimes (see Ni et al. 2017, their Fig. 8). The microwave-only AMSU-B climatology of Ferraro et al. (2015), which extends to 60° latitude, exhibits a high representation of hail in Greenland (see their Fig. 12). The radar-based (DPR) climatology of Mroz et al. (2017) does not exhibit estimated hail in sea ice regimes, as a surface signature would not affect a radar instrument. We exploited this relationship to construct a snow and ice surface regime filter in section 4b and Fig. 5.

In both panels of Fig. 6, note the profusion of hail events as estimated over equatorial Africa, and the Sahel. This hot spot occurs in other passive microwave–based climatologies, like the microwave-only climatology

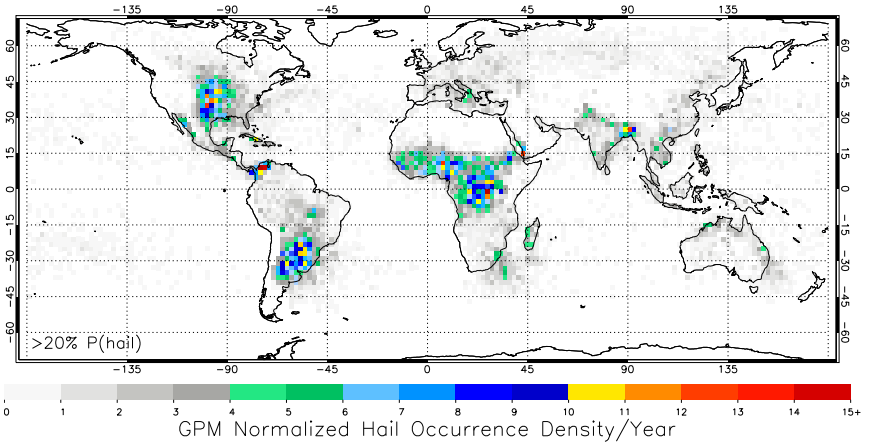

FIG. 7. Climatology of hail in the GPM domain from April 2014 to March 2018. Values are of accumulated probability of hail (>20%) as estimated using minimum 19-GHz PCT and normalized 37-GHz PCT depression [Eq. (2)]. The 19-GHz PCT has been histogram-adjusted to account for the difference in footprint of the GMI instrument used for the climatology and the TMI instrument used to create the algorithm [Eq. (3)]. This climatology has been subjected to the snow/ice filter we propose in section 4b, normalized for overpasses and area (section 4c), and averaged into 2° × 2° boxes for smoothness.

of Ni et al. (2017, their Fig. 8a) and Ferraro et al. (2015, their Fig. 12e). In the climatology of Cecil and Blankenship (2012, their Fig. 6b), equatorial Africa also exhibits a high estimated frequency of hail, however, they impose a regional correction to address this. As the amount of scattering by ice particles within the column also depends on the depth of the vertical layer with those particles, a deep layer of smaller (<~20 mm) ice particles may exhibit a similarly low T_b to a shallower layer of larger hail sized particles. In the deep tropics (such as equatorial Africa), the high tropopause may support an especially deep layer of ice particles.

Radar-based climatologies, like that of Ni et al. (2017, their Fig. 8b) have a dampened hail response in central/equatorial Africa relative to the microwave-based climatology, suggesting that the particles scattering the microwave radiation are less often large hail. The hail retrieval of Mroz et al. (2017, their Fig. 7a), although radar (DPR) based, is trained on dual-polarization ground-radar-based particle identification, the use of which as "ground truth" does not require hail to have reached the ground, and may therefore include particles that are small hail aloft in the cloud, but are not hail at the surface. To address the large representation of hail in equatorial Africa that we suspect is not manifested as large hail reaching the ground, we normalize the extent of the scattering in the 37-GHz channel (as determined by its T_b depression) by the depth of the troposphere [Eq. (2)].

The climatology presented in Fig. 7 is subjected to the snow/ice filter as in Fig. 6b. However, the hail frequencies in Fig. 7 use 37-GHz PCT depression, instead of using the minimum 37-GHz PCT as in Fig. 6. That is, Fig. 7 accounts for the magnitude of the 37-GHz depression relative to a background value, instead of simply using the minimum PCT value. Although in Fig. 6b the cold high-latitude icy regimes no longer present an issue because of the snow/ice filtering and the different regressed variable, there remains a high concentration of estimated hail in the Sahel and central Africa.

In Fig. 7, the 37-GHz PCT depression is normalized by the tropopause height as in Eq. (2). This decreases the representation of hail in central Africa in particular, relative to other hot spots such as the central United States, northern Argentina into Brazil, Uruguay, and Paraguay, and eastern India into Bangladesh remain constant through all three panels of Figs. 6 and 7, no matter which filtering or normalization is applied.

The climatology in Fig. 7, in which we use of both minimum 19-GHz PCT and normalized 37-GHz PCT depression to estimate probability of hail, represents our best estimate of hail within the GPM domain. Snow and ice regimes are downplayed and the regional effect of deep tropospheres in the tropics is mitigated. Very few severe hailstorms are suggested over oceans, and those are primarily over warm waters within a few hundred kilometers of active continental regions (e.g., the Gulf of Mexico, offshore from Uruguay and southern Brazil, and offshore from South Africa). The contrast between subtropical hot spots and the deep tropics appears more realistic than in the earlier figures or some other passive microwave–based climatologies, and better agrees with

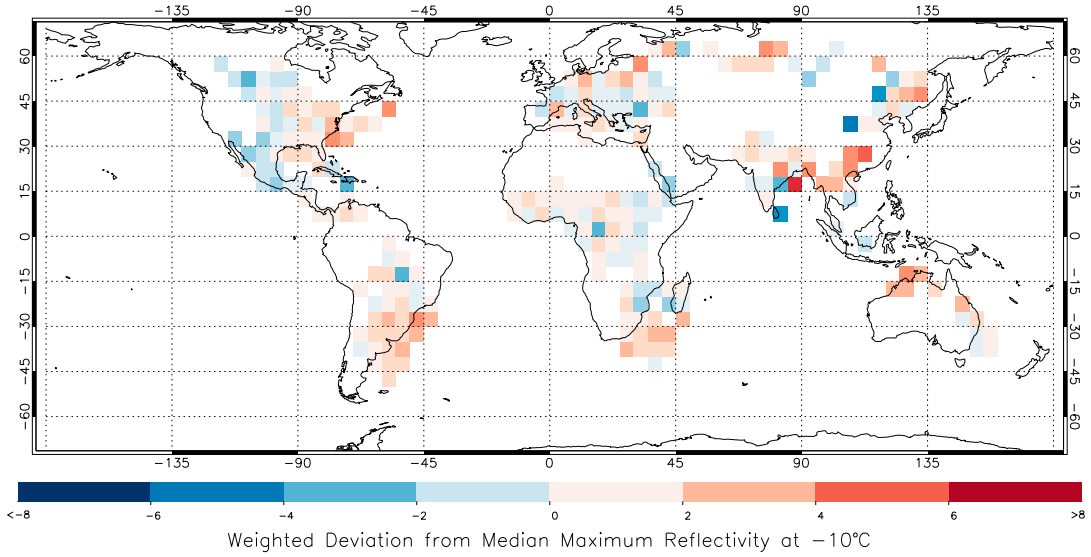

FIG. 8. Map of the weighted deviation from median maximum GPM DPR Ku-band reflectivity at −10°C for GPCTFs whose estimated probability of hail is ≥ 20% in 5° grid boxes. The median reflectivity is estimated as a function of the estimated probability of hail, as calculated from minimum 19-GHz PCT and normalized 37-GHz PCT depression: *P*(hail). The median value is subtracted from the GPCTF value, which is then weighted by the *P*(hail). Positive values (red) indicate that the PCTF's maximum reflectivity at −10°C exceeds the median value or that the storm appears stronger to the DPR than it does to our GMI-based hail-estimation approach. Negative values (blue) indicate that the GMI-based approach is overestimating the strength of the storm, relative to the DPR.

radar-based approaches. It avoids the artificial scaling at set geographical boundaries that Cecil and Blankenship (2012) employed to make the deep tropics appear more realistic. Unlike radar-based approaches, the approach taken here can be applied to large datasets from several wide-swath passive microwave imagers.

6. Validation using GPM radar

Any near-global climatology of hail or other severe storm types can be questioned about the potential for region-dependent biases. We evaluate this by again using the subset of GPCTFs from within the Ku-band radar swath of the GPM DPR, as we used in section 4b. For those features, we use their maximum radar reflectivity at the −10°C level. We grouped those GCPTFs by hail probability, and then determined the median value of maximum radar reflectivity as a function of GMI-derived hail probability. We then compute the deviation from this "expected" reflectivity value for each individual GPCTF. A positive deviation means that the storm appears stronger to the radar than it does to our GMI-based approach.

Those deviations from the expected radar reflectivity values at −10°C are weighted by the GMI-based hail probabilities and averaged in Fig. 8. This mimics the weighting by hail probability that is used in accumulating our estimated hail climatology in Fig. 7. The purpose of Fig. 8 is to assess whether our climatology is likely to have consistent, meaningful regional biases. As such, the calculations for Fig. 8 use a coarser-resolution (5°) grid, and grid boxes with very low accumulated hail probabilities (<20%) are omitted.

In general, the deviations mapped in Fig. 8 are small, suggesting confidence in the relative patterns seen in Fig. 7. The largest consistent positive deviations in Fig. 8 are across Southeast Asia and eastern China, suggesting that Fig. 7 may slightly underestimate the frequency of hail there. There is also a hint of potential underestimation for northern Australia, and off the coasts of South Africa and southeastern South America, with potential overestimation across Mexico. That being said, the results in Fig. 8 strengthen our confidence in the climatology we present in Fig. 7.

7. Summary

The use of spaceborne passive microwave radiometry for the training of hail retrievals provides an opportunity for uniform detection and global coverage of hail estimates that ground reports and ground-based radar networks alone cannot supply. In this paper, we pair Tropical Rainfall Measuring Mission (TRMM) polarization corrected temperature precipitation features (TPCTFs) over the United States with ground hail reports to train a hail retrieval algorithm to

estimate the probability of hail given a TPCTF's suite of different microwave brightness temperatures.

Scattering of upwelling microwave radiation by ice particles within the column (manifested as a depression in T_b) has become a well-accepted proxy for severe precipitation, including hail. We fit logistic curves to the probability of hail associated with several variables from passive microwave channels from 10 to 85 GHz. We find that two variables in particular produce realistic climatologies: the minimum 19-GHz PCT and normalized 37-GHz PCT depression [maximum 37-GHz PCT − minimum 37-GHz PCT, normalized by the height of the troposphere; Eq. (2)]. By using multiple microwave frequencies in combination, we can leverage as much information as possible from a single TPCTF about the concentration and size of scatterers within the column. We then apply this method to all PCTFs in the Global Precipitation Measurement satellite (GPCTFs) in the extended domain from 69°S to 69°N to develop a climatology for the 4-yr period between April 2014 and March 2018.

Because the GPM satellite samples higher latitudes and more ice- and snow-covered regimes than did the TRMM satellite, the radiative properties of these regimes poses challenges for retrieving likely hailing precipitation GPCTFs. We find that exploiting the difference between the 10-GHz PCT and 89-GHz PCT depressions [see Eq. (4)] proves to be an effective filter for ice and snow regimes that are registering in the retrieval as hail, but are not actually likely hailing GPCTFs.

We present a climatology of accumulated estimated probability of hail using minimum 19-GHz PCT and normalized 37-GHz PCT depression, calculated as normalized estimated hail events per year, in Fig. 7. To account for differences in footprint sizes of the microwave imagers on board the two different satellites, we employ a histogram-matching method to scale the GPM 19-GHz PCTs to the match the distribution of those observed by the TRMM Microwave Imager [Eq. (3)]. We also present climatologies from retrievals based on minimum 37-GHz PCT (Fig. 6) to show some effects of particular components of our method. We find the climatology based on the retrieval using the *normalized 37-GHz PCT depression* together with the *minimum 19-GHz PCT* to be the most realistic.

Our climatology shows the greatest hail frequencies in South America, in the region from northern Argentina into southern Brazil; the central United States; and a swath of Africa just south of the Sahel. Smaller hot spots include Pakistan, and the eastern India/Bangladesh area. Notably, other climatologies in the literature exhibit high concentrations of estimated hail over equatorial and central Africa, especially those climatologies that use solely passive microwave data. We suspect this is due to the increased depth of the troposphere in the tropics and the deeper layers of smaller ice scatterers that can develop therein. The central Africa hot spot does not appear as strongly in regionally corrected passive microwave or radar-based climatologies. When accounting for tropopause height in Fig. 7, the central African hot spot clearly appears diminished relative to the aforementioned regions of subtropical South America, the central United States, and sub-Sahelian Africa, although its estimated hail frequency still exceeds other parts of the world.

We present here three techniques that have not been employed in hail climatologies in the literature: a combination of scattering signatures for both 19 and 37 GHz, normalization of the 37-GHz PCT depression by the height of the tropopause, and a multifrequency parameter for filtering surface snow and ice regimes that are erroneously retrieved as hail. By doing so we have built what we believe is a realistic estimated global climatology of hail from the tropics to the midlatitudes. An initial validation using concurrent radar reflectivity measurements suggests that regional biases in this climatology are small. Using these frequencies, the techniques developed here can be applied to large datasets from multiple satellites dating back to 1997. Modification to exclude the 10-GHz frequency could open this to extension for the Defense Meteorological Satellite Program series of Special Sensor Microwave Imagers, dating back into the late 1980s.

Acknowledgments. The authors are deeply grateful for the efforts of Dr. Chuntao Liu at Texas A&M Corpus Christi for providing and maintaining GPM and TRMM precipitation feature products and making them available for all. We also thank Nana Liu at Texas A&M Corpus Christi for providing the lapse-rate tropopause calculations on the ERA-Interim reanalysis data. We appreciate the insight and comments from our three anonymous reviewers and our editor, all of whose constructive feedback undoubtedly strengthened this paper. The work of S. Bang was supported by an appointment to the NASA Postdoctoral Program at the NASA Marshall Space Flight Center, administered by Universities Space Research Association under contract with NASA. Author D. Cecil's work was supported by NASA's Precipitation Measurement Mission Science Team.

REFERENCES

Allen, J., and M. Tippett, 2015: The characteristics of United States hail reports: 1955–2014. *Electron. J. Severe Storms Meteor.*, **10** (3), http://www.ejssm.org/ojs/index.php/ejssm/article/viewArticle/149.

Aon Benfield, 2018: Global catastrophe recap: First half of 2018. Aon Benfield Analytics and Impact Forecasting Rep., 12 pp.,

http://thoughtleadership.aonbenfield.com/Documents/20180724-ab-analytics-if-1h-global-report.pdf.

Bedka, K. M., 2011: Overshooting cloud top detections using MSG SEVIRI infrared brightness temperatures and their relationship to severe weather over Europe. *Atmos. Res.*, **99**, 175–189, https://doi.org/10.1016/j.atmosres.2010.10.001.

Berg, W., 2016: GPM GMI Common Calibrated Brightness Temperatures Collocated L1C 1.5 hours 13 km, version 05. NASA Goddard Earth Sciences Data and Information Services Center, accessed 2 October 2018, https://doi.org/10.5067/GPM/GMI/GPM/1C/05.

Berrisford, P., and Coauthors, 2011: The ERA-Interim Archive, version 2.0. European Centre for Medium-Range Weather Forecasts Rep., 16 pp., https://www.ecmwf.int/node/8174.

Bluestein, H. B., and S. S. Parker, 1993: Modes of isolated, severe convective storm formation along the dryline. *Mon. Wea. Rev.*, **121**, 1354–1372, https://doi.org/10.1175/1520-0493(1993)121<1354:MOISCS>2.0.CO;2.

Cecil, D. J., 2009: Passive microwave brightness temperatures as proxies for hailstorms. *J. Appl. Meteor. Climatol.*, **48**, 1281–1286, https://doi.org/10.1175/2009JAMC2125.1.

——, 2011: Relating passive 37-GHz scattering to radar profiles in strong convection. *J. Appl. Meteor. Climatol.*, **50**, 233–240, https://doi.org/10.1175/2010JAMC2506.1.

——, and C. B. Blankenship, 2012: Toward a global climatology of severe hailstorms as estimated by satellite passive microwave imagers. *J. Climate*, **25**, 687–703, https://doi.org/10.1175/JCLI-D-11-00130.1.

——, and T. Chronis, 2018: Polarization-corrected temperatures for 10-, 19-, 37-, and 89-GHz passive microwave frequencies. *J. Appl. Meteor. Climatol.*, **57**, 2249–2265, https://doi.org/10.1175/JAMC-D-18-0022.1.

——, S. J. Goodman, D. J. Boccippio, E. J. Zipser, and S. W. Nesbitt, 2005: Three years of TRMM precipitation features. Part I: Radar, radiometric, and lightning characteristics. *Mon. Wea. Rev.*, **133**, https://doi.org/10.1175/MWR-2876.1.

Changnon, S. A., 2009: Increasing major hail losses in the U.S. *Climatic Change*, **96**, 161–166, https://doi.org/10.1007/s10584-009-9597-z.

Cintineo, J. L., T. M. Smith, V. Lakshmanan, H. E. Brooks, and K. L. Ortega, 2012: An objective high-resolution hail climatology of the contiguous United States. *Wea. Forecasting*, **27**, 1235–1248, https://doi.org/10.1175/WAF-D-11-00151.1.

Dee, D., and Coauthors, 2011: The ERA-Interim reanalysis: Configuration and performance of the data assimilation system. *Quart. J. Roy. Meteor. Soc.*, **137**, 553–597, https://doi.org/10.1002/qj.828.

Dolan, B., and S. A. Rutledge, 2009: A theory-based hydrometeor identification algorithm for X-band polarimetric radars. *J. Atmos. Oceanic Technol.*, **26**, 2071–2088, https://doi.org/10.1175/2009JTECHA1208.1.

Ebtehaj, A. M., and C. D. Kummerow, 2017: Microwave retrievals of terrestrial precipitation over snow-covered surfaces: A lesson from the GPM satellite. *Geophys. Res. Lett.*, **44**, 6154–6162, https://doi.org/10.1002/2017GL073451.

ECMWF, 2018: ECMWF ERA-Interim, daily. ECMWF, accessed 18 September 2018, https://apps.ecmwf.int/datasets/data/interim-full-daily.

Ferraro, R., J. Beauchamp, D. Cecil, and G. Heymsfield, 2015: A prototype hail detection algorithm and hail climatology developed with the Advanced Microwave Sounding Unit (AMSU). *Atmos. Res.*, **163**, 24–35, https://doi.org/10.1016/j.atmosres.2014.08.010.

Griffin, S. M., K. M. Bedka, and C. S. Velden, 2016: A method for calculating the height of overshooting convective cloud tops using satellite-based IR imager and *CloudSat* cloud profiling radar observations. *J. Appl. Meteor. Climatol.*, **55**, 479–491, https://doi.org/10.1175/JAMC-D-15-0170.1.

Grody, N. C., 1991: Classification of snow cover and precipitation using the special sensor microwave imager. *J. Geophys. Res.*, **96**, 7423–7435, https://doi.org/10.1029/91JD00045.

Hohl, R., H.-H. Schiesser, and D. Aller, 2002: Hailfall: The relationship between radar-derived hail kinetic energy and hail damage to buildings. *Atmos. Res.*, **63**, 177–207, https://doi.org/10.1016/S0169-8095(02)00059-5.

Hou, A. Y., and Coauthors, 2014: The Global Precipitation Measurement Mission. *Bull. Amer. Meteor. Soc.*, **95**, 701–722, https://doi.org/10.1175/BAMS-D-13-00164.1.

Iguchi, T., and R. Meneghini, 2016: GPM GMI (GPROF) Radiometer Precipitation Profiling L2A 1.5 hours 13 km, version 05. NASA Goddard Earth Science Data and Information Services Center, accessed 2 October 2018, https://doi.org/10.5067/GPM/GMI/GPM/GPROF/2A/05.

Johns, R., and J. Hart, 1998: The occurrence and non-occurrence of large hail with strong and violent tornado episodes: Frequency distributions. Preprints, *19th Conf. on Severe Local Storms*, Minneapolis, MN, Amer. Meteor. Soc., 283–286.

Kummerow, C., W. Barnes, T. Kozu, J. Shiue, and J. Simpson, 1998: The Tropical Rainfall Measuring Mission (TRMM) sensor package. *J. Atmos. Oceanic Technol.*, **15**, 809–817, https://doi.org/10.1175/1520-0426(1998)015<0809:TTRMMT>2.0.CO;2.

Leppert, K. D., and D. J. Cecil, 2015: Signatures of hydrometeor species from airborne passive microwave data for frequencies 10–183 GHz. *J. Appl. Meteor. Climatol.*, **54**, 1313–1334, https://doi.org/10.1175/JAMC-D-14-0145.1.

Liu, C., E. J. Zipser, D. J. Cecil, S. W. Nesbitt, and S. Sherwood, 2008: A cloud and precipitation feature database from nine years of TRMM observations. *J. Appl. Meteor. Climatol.*, **47**, https://doi.org/10.1175/2008JAMC1890.1.

Liu, N., and C. Liu, 2018: Synoptic environments and characteristics of convection reaching the tropopause over northeast China. *Mon. Wea. Rev.*, **146**, 745–759, https://doi.org/10.1175/MWR-D-17-0245.1.

Mroz, K., A. Battaglia, T. J. Lang, D. J. Cecil, S. Tanelli, and F. Tridon, 2017: Hail-detection algorithm for the GPM *Core Observatory* satellite sensors. *J. Appl. Meteor. Climatol.*, **56**, 1939–1957, https://doi.org/10.1175/JAMC-D-16-0368.1.

——, ——, ——, S. Tanelli, and G. F. Sacco, 2018: Global precipitation measuring dual-frequency precipitation radar observations of hailstorm vertical structure: Current capabilities and drawbacks. *J. Appl. Meteor. Climatol.*, **57**, 2161–2178, https://doi.org/10.1175/JAMC-D-18-0020.1.

Murillo, E. M., and C. R. Homeyer, 2019: Severe hail fall and hailstorm detection using remote sensing observations. *J. Appl. Meteor. Climatol.*, **58**, 947–970, https://doi.org/10.1175/JAMC-D-18-0247.1.

Nesbitt, S. W., E. J. Zipser, and D. J. Cecil, 2000: A census of precipitation features in the tropics using TRMM: Radar, ice scattering, and lightning observations. *Mon. Wea. Rev.*, **13**, 4087–4106, https://doi.org/10.1175/1520-0442(2000)013<4087:ACOPFI>2.0.CO;2.

Ni, X., C. Liu, D. J. Cecil, and Q. Zhang, 2017: On the detection of hail using satellite passive microwave radiometers and precipitation radar. *J. Appl. Meteor. Climatol.*, **56**, 2693–2709, https://doi.org/10.1175/JAMC-D-17-0065.1.

PPS, 2014: Tropical Rainfall Measuring Mission Level 1Z, version 7. Texas A&M University, accessed 20 December 2018, http://atmos.tamucc.edu/trmm/data/trmm/level_1/.

Punge, H. J., K. M. Bedka, M. Kunz, and A. Reinbold, 2017: Hail frequency estimation across Europe based on a combination of overshooting top detections and the ERA-INTERIM reanalysis. *Atmos. Res.*, **198**, 34–43, https://doi.org/10.1016/j.atmosres.2017.07.025.

Schlie, E. E.-J., D. Wuebbles, S. Stevens, R. Trapp, and B. Jewett, 2019: A radar-based study of severe hail outbreaks over the contiguous United States for 2001–2011. *Int. J. Climatol.*, **39**, 278–291, https://doi.org/10.1002/joc.5805.

Scott, D. W., 1979: On optimal and data-based histograms. *Biometrika*, **66**, 605–610, https://doi.org/10.1093/biomet/66.3.605.

Skofronick-Jackson, G., and B. T. Johnson, 2011: Surface and atmospheric contributions to passive microwave brightness temperatures for falling snow events. *J. Geophys. Res.*, **116**, D02213, https://doi.org/10.1029/2010JD014438.

Spencer, R. W., M. R. Howland, and D. A. Santek, 1987: Severe storm identification with satellite microwave radiometry: An initial investigation with *Nimbus-7* SMMR data. *J. Climate Appl. Meteor.*, **26**, 749–754, https://doi.org/10.1175/1520-0450(1987)026<0749:SSIWSM>2.0.CO;2.

——, H. M. Goodman, and R. E. Hood, 1989: Precipitation retrieval over land and ocean with the SSM/I: Identification and characteristics of the scattering signal. *J. Atmos. Oceanic Technol.*, **6**, 254–273, https://doi.org/10.1175/1520-0426(1989)006<0254:PROLAO>2.0.CO;2.

Toracinta, E. R., D. J. Cecil, E. J. Zipser, and S. W. Nesbitt, 2002: Radar, passive microwave, and lightning characteristics of precipitating systems in the tropics. *Mon. Wea. Rev.*, **130**, 802–824, https://doi.org/10.1175/1520-0493(2002)130<0802:RPMALC>2.0.CO;2.

Vivekanandan, J., J. Turk, and V. N. Bringi, 1991: Ice water path estimation and characterization using passive microwave radiometry. *J. Appl. Meteor.*, **30**, 1407–1421, https://doi.org/10.1175/1520-0450(1991)030<1407:IWPEAC>2.0.CO;2.

World Meteorological Organization, 1957: Meteorology—A three-dimensional science: Second session of the Commission for Aerology. *WMO Bull.*, **6**, 134–138, https://library.wmo.int/pmb_ged/bulletin_6-4_en.pdf.

Xie, B., Q. Zhang, and Y. Wang, 2008: Trends in hail in China during 1960–2005. *Geophys. Res. Lett.*, **35**, L13801, https://doi.org/10.1029/2008GL034067.